Original Article
Bulletin of Pure and Applied Sciences.
Chemistry , Vol.44 C, No.1
January-June 2025: P.40-60

http://www.bpasjournals.com/chemistry
Print version ISSN 0970 4620
Online version ISSN 2320 320X

Hydrogen Evolution by Photocatalytic Water Splitting with Novel Bimetallic Metal-organic frameworks Without Cocatalysts

[1]Anjali Anand, [1]Sreevidya M.S. and [1,2,3]Rani Pavithran[*]

Author's Affiliations:
[1]Department of Chemistry, University College, Thiruvananthapuram, Kerala 695034, India.
[2]Department of Chemistry, College of Engineering Trivandrum, Thiruvananthapuram, Kerala 695016, India.
[3]Centre for sustainable Development, College of Engineering Trivandrum, Kerala 695016, India

***Corresponding Author: Rani Pavithran,** Department of Chemistry, University College, Thiruvananthapuram, Kerala 695034, India.
E-mail: ranipavithran@gmail.com

ABSTRACT

Three bimetallic metal organic frameworks of transition metal ions were synthesized by solvothermal method using 1,4-benzenedicarboxylic acid as the ligand and their photocatalytic efficiency for the production of hydrogen by water splitting was investigated under visible light irradiation. They were analyzed with infrared, PXRD, SEM, EDS, UV-vis and PL analysis.

Keywords: Metal Organic Framework, Solvothermal Synthesis, 1,4-Benzenedicarboxylic Acid, Water Splitting, Hydrogen Evolution.

Received on 02.01.2025, Revised on 20.04.2025, Accepted on 12.05.2025

How to cite this article: Anand A., Sreevidya M.S. and Pavithran R. (2025). Hydrogen Evolution by Photocatalytic Water Splitting with Novel Bimetallic Metal-organic frameworks Without Cocatalysts. *Bulletin of Pure and Applied Sciences-Chemistry*, 44C (1), 40-60.

INTRODUCTION

MOFs are produced by the combination of metal centers and organic ligands, forming one-, two-, or three-dimensional coordination networks [1]. Their high surface area and porosity, veracity of structure, as well as tunable pore surface properties make them suitable for various applications [2]. MOFs have also emerged as promising candidates for photocatalysis, especially for H_2 production through water splitting [3-5]. Here we introduce three MOFs and three novel bimetallic MOF photocatalysts for effective water splitting without any cocatalyst.

Chemicals and Instrumentation

Chemicals

A.R grade chromium chloride, zirconium oxychloride & ferrous sulphate were employed as metal sources. Benzene-1,4-dicarboxylic acid (BDC) and methanol were utilised as ligand and solvent, respectively. Chemicals were not subjected to further purification.

Instrumentation

Synthesis of MOFs

1 mmol of metal salt [zirconium oxychloride for Zr BDC MOF, chromium chloride for Cr BDC MOF and ferrous sulphate for Fe BDC MOF] and 1mmol of 1,4-BDC were combined thoroughly in 10 mL of methanol. The mixture was heated in an autoclave at 150^0C for 72 hours. It was cooled, filtered and washed with methanol. The MOF was dried in a desiccator over silica crystals. Also, the heterobimetallic MOFs were synthesized by mixing salts of two different metals (Fe & Cr; Zr & Cr; Zr & Fe) in 1:1 molar ratio with 1 mmol BDC in 10 ml of methanol.

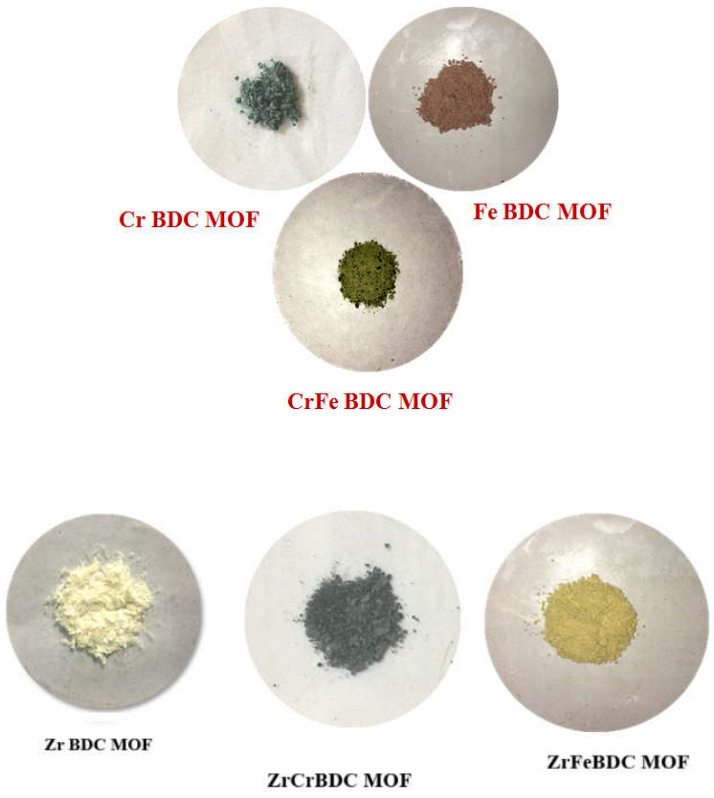

Figure 1: Photographs of synthesized MOFs

Photo catalytic activity studies

In the present study solar stimulator method is used. Apparatus consists of a cell kit, solar cell, magnetic stirrer and 10 ml measuring jar. About 0.2g of sample was taken in cell kit and 20 ml of water was added and made air tight. It is continuously stirred by magnetic stirrer throughout the experiment. Solar cell is adjusted such that rays fall completely on the cell kit. The capillary tube of cell kit is maintained inside the measuring jar filled with water.

Characterization methods

Powder X-Ray diffraction data for the prepared MOFs was collected on a BRUKER D8 advance X-ray Diffractometer by Cu–Kα radiation with a wavelength of 1.5418 Å at 30 KV and 10 mA. Fourier transform infra-red (FTIR) spectrum was done using Perkin Elmer FT-IR spectrophotometer with KBr pellets. Carl Zeiss EVO 18 FE-SEM with EDS was used for collecting the scanning electron microscopy (SEM) images. The solid UV-Visible studies were recorded using Cary 5000 high performance UV-Vis-NIR spectrometer. JASCO Spectrofluorometer FP-8300 was used for recording the photo-

luminescence spectra. Photocatalytic studies were carried out through solar simulator.

RESULTS AND DISCUSSION

Infrared Spectral Analysis

In the infrared spectra, broad band at 3179 cm^{-1} in Cr BDC MOF (Fig.3); at 3334.5 cm^{-1} in Fe BDC MOF (Fig.4); at 3427.5 cm^{-1} in the hetero bimetallic Cr Fe BDC MOF (Fig.5); at 2961.4 cm^{-1} in Zr BDC MOF (Fig.6); at 3369.4 cm^{-1} in Zr Fe BDC MOF (Fig.7): and at 3219.2 cm^{-1} in Zr Cr BDC MOF (Fig.8) correspond to hydroxyl group of ethanol solvent and stretching of OH bond with the metal. C=O stretching band at 1674.04 in the ligand (Fig.2) was shifted to 1670.6 cm^{-1} in Cr BDC MOF; to 1686.16 cm^{-1} in Fe BDC MOF; to 1710.5 cm^{-1} in Zr BDC MOF; to 1639.7 cm^{-1} in Cr Fe BDC MOF; to 1656.7 cm^{-1} in Cr Zr BDC MOF and to 1674.5 cm^{-1} in ZrFe BDC MOF showing that COOH moiety is present and there is interaction between the metal and the COOH moiety in these MOFs. IR spectra of the synthesized MOFs of Zr, Cr and Fe showed similar C=O stretching band between 1720 – 1630 cm^{-1} and symmetric C-O stretching between 1390 and 1440 as reported elsewhere [6].

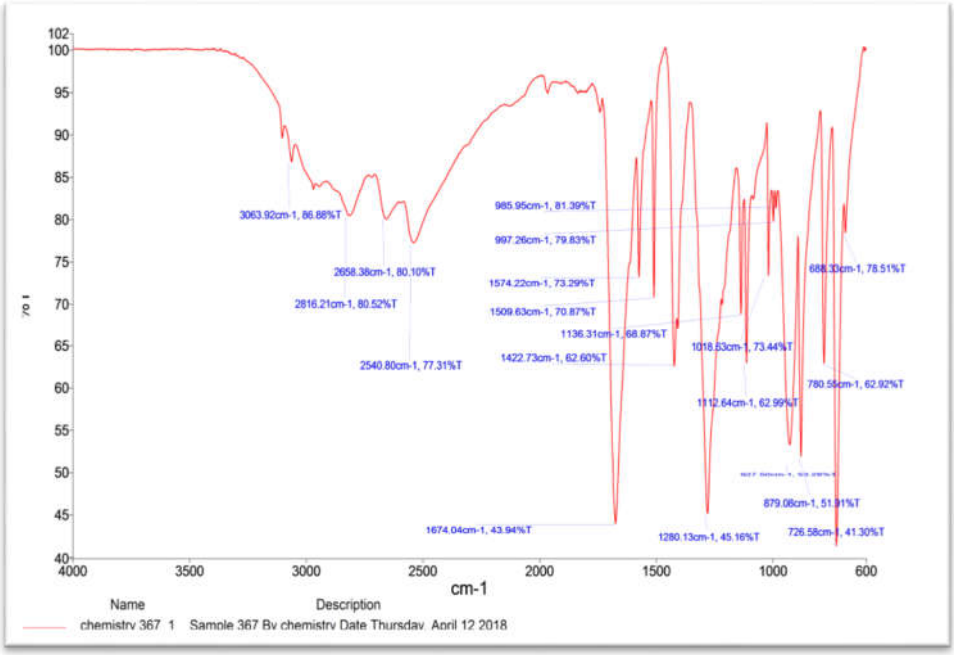

Figure 2: IR spectrum of ligand

In the infrared spectra of MOFs, there was a shift in frequency from 930 cm^{-1} in the ligand to 926 cm^{-1} in Cr BDC MOF, to 930 cm^{-1} in Fe BDC MOF; to 926 cm^{-1} in CrFe BDC MOF; to 954.39 cm^{-1} in ZrBDC MOF; to 884.90 cm^{-1} in ZrFe BDC MOF; to 954.39 cm^{-1} in ZrCr BDC MOF showing the presence of dimeric carboxylic group [7, 8]. Intense bands at 524.6 cm^{-1} in Fe BDC MOF; at 571.09 cm^{-1} in Cr Fe BDC MOF; at 780 cm^{-1} in Zr BDC MOF; 780.16 and 502.36 cm^{-1} in ZrFe BDC MOF; at 775.6 & 657.7 cm^{-1} in ZrCr BDC MOF clearly indicate metal-oxygen symmetric stretch further proving the co-ordination of metal to the carboxylate group of the ligand [6-8] (Fig.3-8) (Table 1).

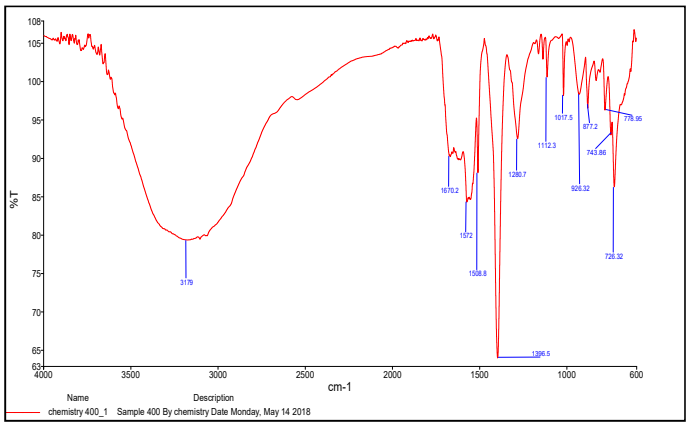

Figure 3: IR spectrum of Cr MOF

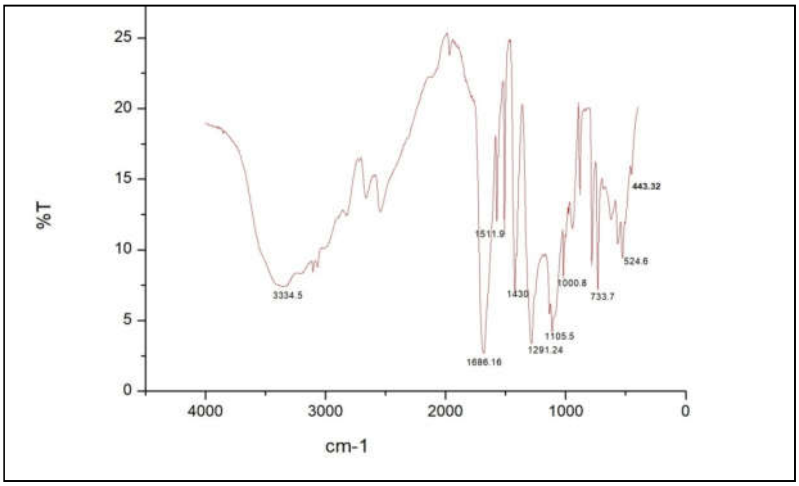

Figure 4: Infrared spectrum of Fe MOF

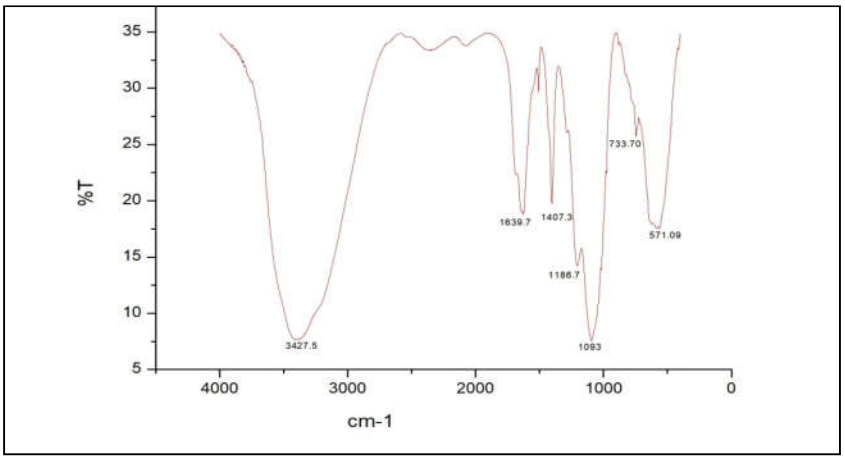

Figure 5: Infrared spectrum of Cr Fe MOF

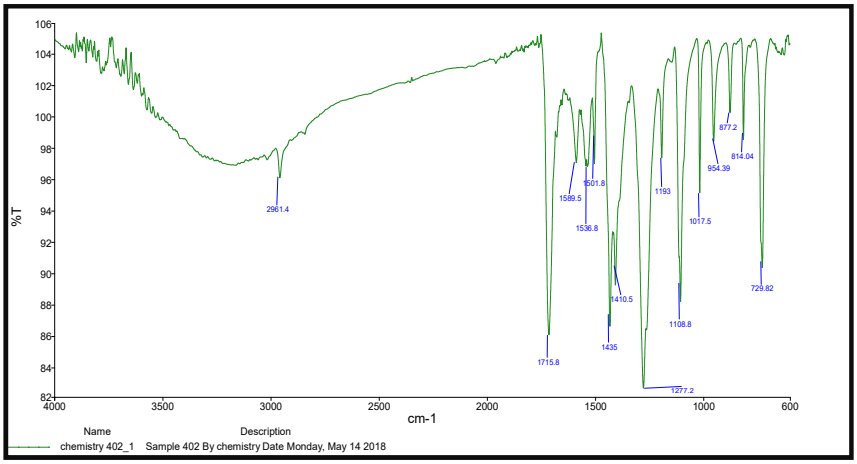

Figure 6: Infrared spectrum of Zr MOF

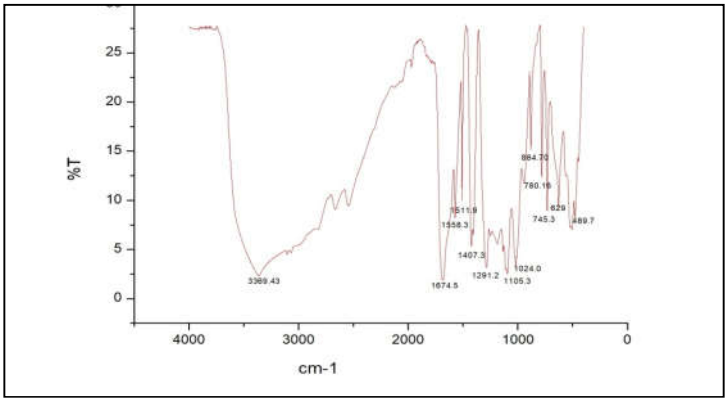

Figure 7: Infrared spectrum of hetero bimetallic Zr Fe MOF

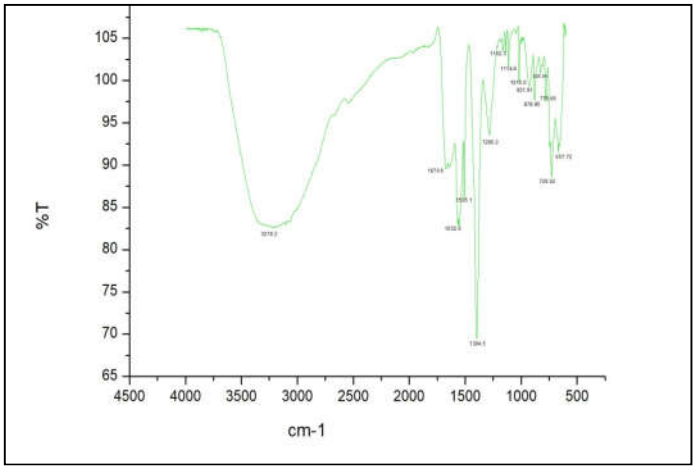

Figure 8: IR spectrum of heterobimetallic Cr Zr MOF

Table 1: Infrared spectral data of MOFs

Peak Assignment	Ligand	Zr BDC MOF	Cr BDC MOF	ZrCr BDC MOF	Fe BDC MOF	ZrFe BDC MOF	CrFe BDC MOF
co-ordinate hydroxyl group and water molecule	3063.92	2961.4	3179	3219.2	3334.5	3369.4	3427.5
C=O bond vibration	1674.04	1715.8	1670	1670.6	1686.16	1674.5	1639.7
Symmetric C=O stretching	1422.73	1435 1410.5	1396.5	1394.5	1430	1407.3	1407.3
Deformation vibration of benzene	1136.31	1108.8	1112	1114.8	1105.5	1105.3	1186.7
C-H bending of ring	726.58 780.55	729.82 780	726.3 778.9	775.6	733.7	745.3 780.1	733.7
Skeletal vibration of benzene ring	1509.63 1574.22	1589.5 1536.8	1572 1508.8	1552.6	1511.9	1558.3	1525.8

Powder x-ray diffraction (PXRD) Results

Sharp diffraction peaks in the XRD pattern indicate the crystalline nature of MOFs (Figs. 9-11). In the PXRD of Cr BDCMOF (Fig.9), the high intensity Bragg diffraction peaks were observed at 2θ= 27.72, 16.80, 25.16, 31.20, 34.69 and 40.96^0.

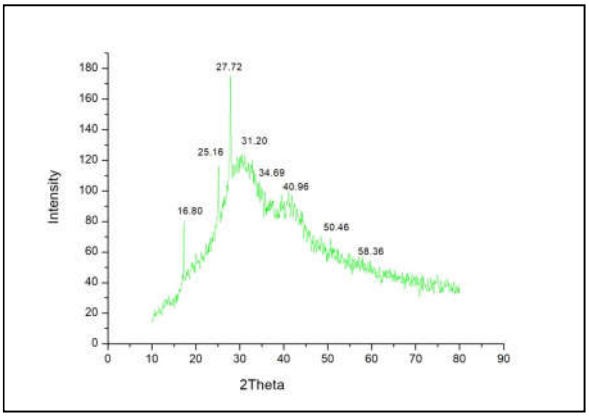

Figure 9: **PXRD of Cr-BDC MOF**

In the PXRD pattern of Fe BDCMOF (Fig.10), the high intensity Bragg diffraction peaks were observed at 2θ= 27.97, 18.19, 22.14, 23.77, 24.93, 32.83 and 39.33^0. In Cr Fe BDCMOF, (Fig.11) the high intensity Bragg diffraction peaks were observed at 2θ=28.86, 17.26, 23.77, 17.96, 33.52, 46.28 and 50.23^0. The average grain sizes were calculated as 378.01 nm, 378.06 nm and 118.69 nm for Cr BDC MOF, for Fe BDC MOF and for Cr Fe BDC MOF, respectively, from Scherrer equation.

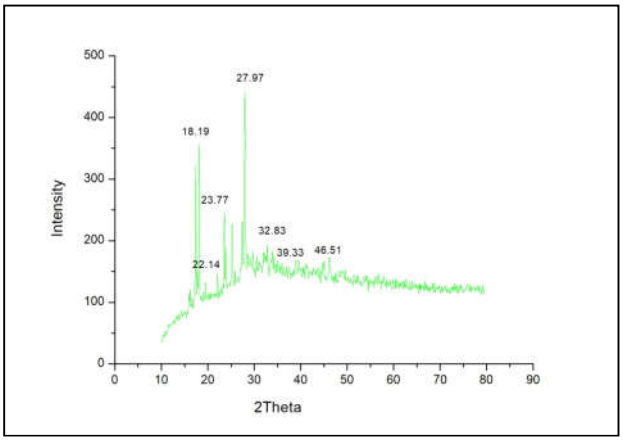

Figure 10: **PXRD of Fe BDC MOF**

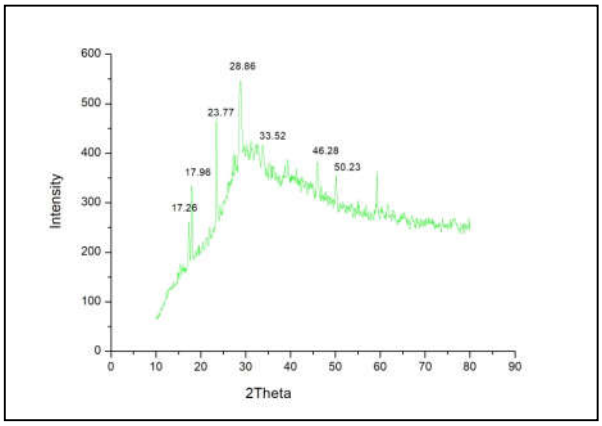

Figure 11: **PXRD pattern of Cr Fe BDC MOF**

The high intensity Bragg diffraction peaks were observed at 2θ=41.60, 42.49, 44.42, 49.53, 58.83, 40.49, 34.69 and 30.74^0 in Zr BDC MOF (Fig. 12). The average grain size calculated was 171.04nm. The PXRD pattern indicated that Zr BDC MOF is amorphous in nature.

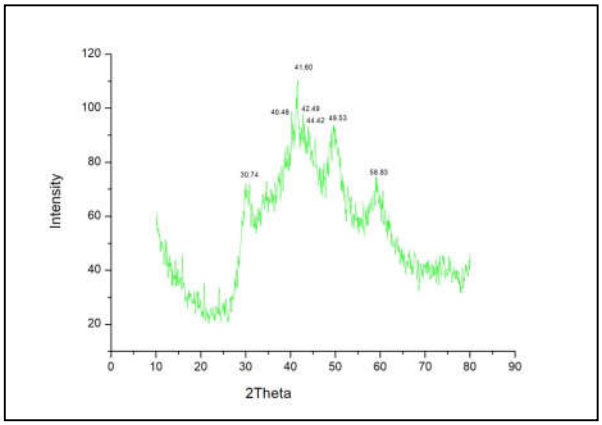

Figure 12: **PXRD pattern of Zr BDC MOF**

In Zr Cr BDCMOF, (Fig.13), the high intensity Bragg diffraction peaks were observed at 2θ= 27.91, 17.03, 25.16, 27.91, 29.34, 32.83, 41.42 and 43.49^0. The average grain size was calculated as 252 nm and the MOF is crystalline in nature as indicated by the sharp peaks.

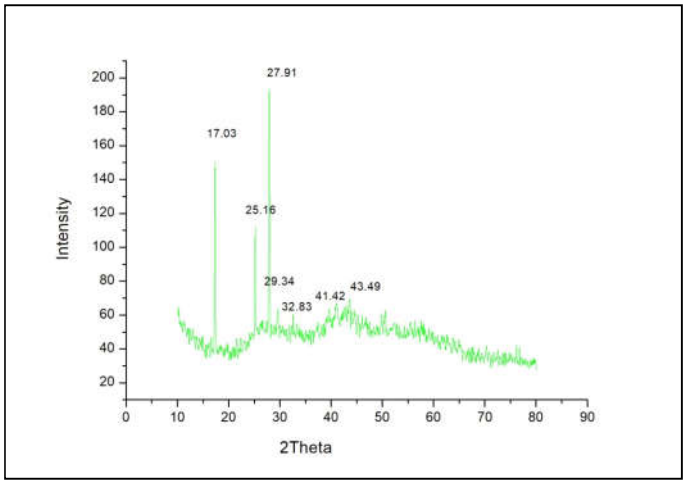

Figure 13: **PXRD pattern of Zr Cr BDC MOF**

In the PXRD of Zr Fe BDCMOF (Fig.14), the high intensity Bragg diffraction peaks were observed at 2θ= 17.94, 23.54, 28.65, 29.81, 31.90, 34.22, 37.01 and 42.54^0. The average grain size calculated was 398.29nm.

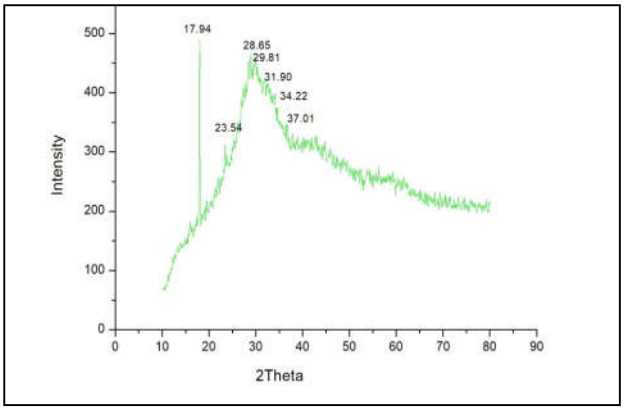

Figure 14: **PXRD pattern of Zr Fe BDC MOF**

SEM Images

Cr BDC MOF (Fig.15 a) showed a waxy sheet like morphology with micro size and that of Fe BDC MOF (Fig.15 b) showed a rectangular morphology with micro size. Cr Fe BDC MOF is micro porous and has a chaotic morphology (Fig.15c). Zr BDC MOF (Fig.16) has a thread like morphology with micro size. The SEM image of Zr Cr BDC MOF (Fig.17) showed a flake like morphology with micro size and that of Zr Fe BDC MOF (Fig.18) showed a sheet like morphology with micro size.

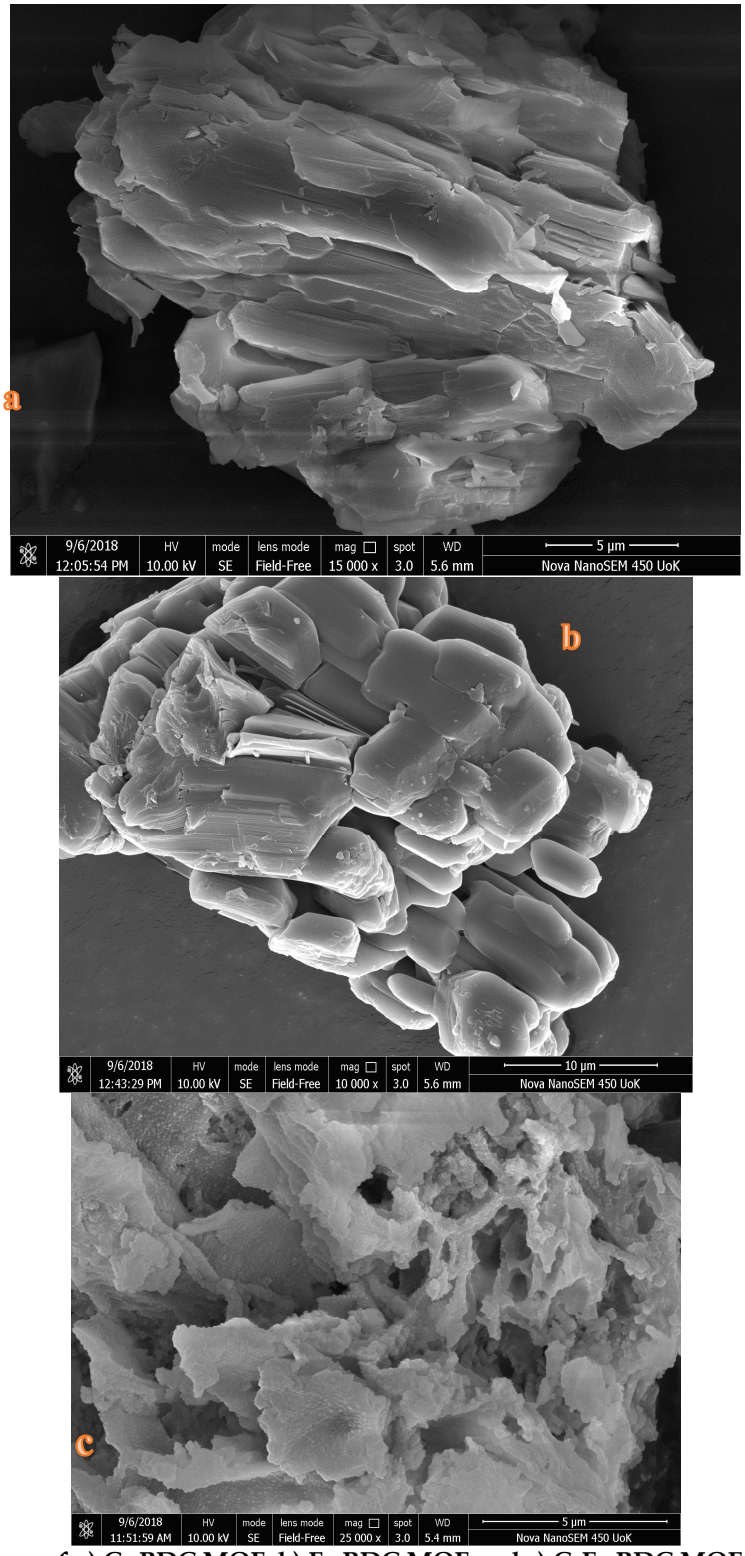

Figure 15: SEM images of a) Cr BDC MOF, b) Fe BDC MOF and c) CrFe BDC MOF

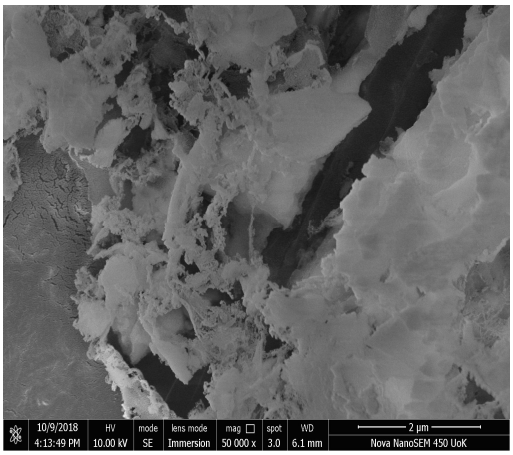

Figure 16: **SEM image of Zr BDC MOF in 2µm**

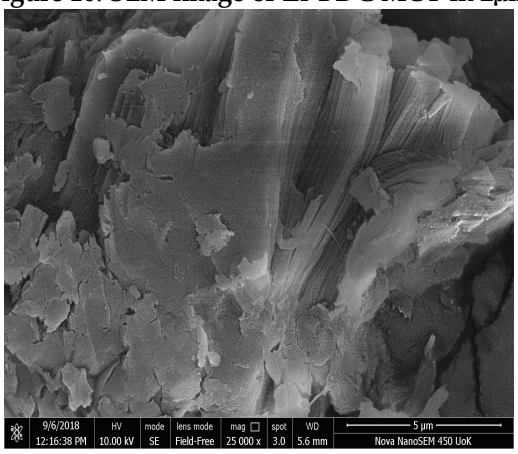

Figure 17: SEM images of Zr Cr BDC MOF in 5 µm

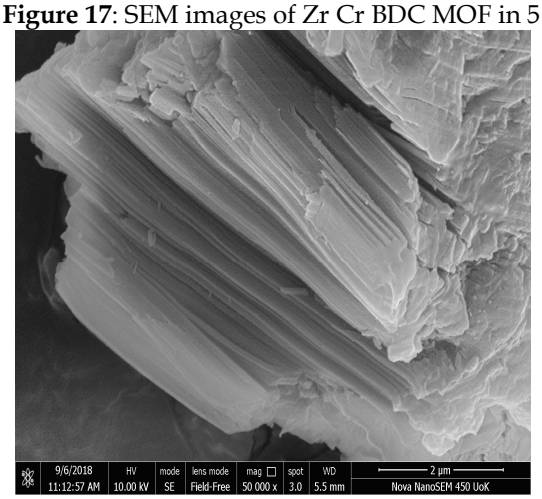

Figure 18: SEM images of Zr FeBDC MOF in 2 µm

Energy dispersive spectroscopic Studies

The EDS of MOFs depicted the presence of chromium, iron and all other expected elements confirming the formation of MOFs (Figs.19a-c). EDS of Zr BDC MOF (Fig 20), Zr Cr BDC MOF (Fig.21) and Zr Fe BDC MOF (Fig.22) showed the presence of the corresponding metals and all other expected elements indicating the successful syntheses of these MOFs. Table 2 gives the EDS results of atomic percentage of various elements in these MOFs.

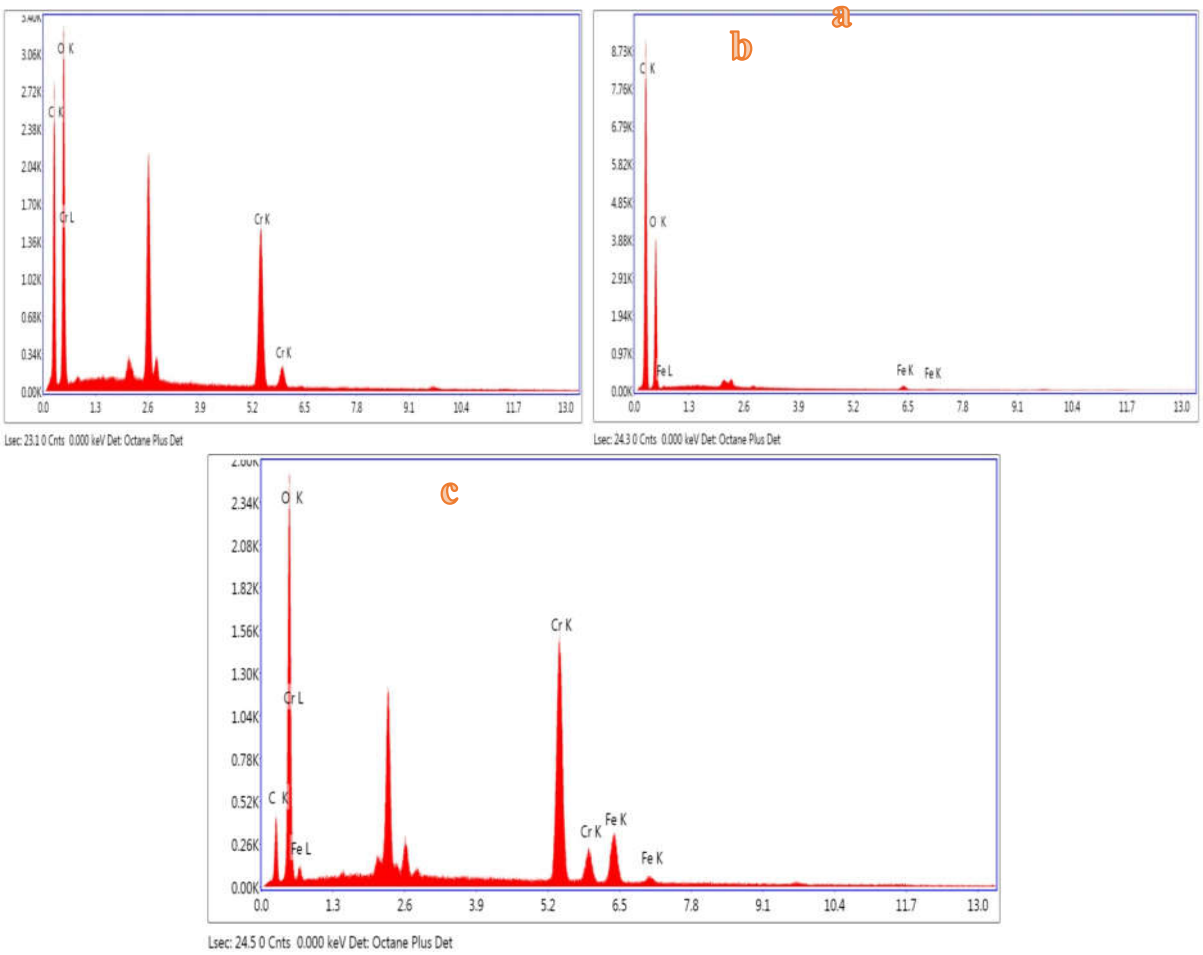

Figure 19: EDS of a) Cr MOF b) Fe MOF and c) Cr Fe MOF

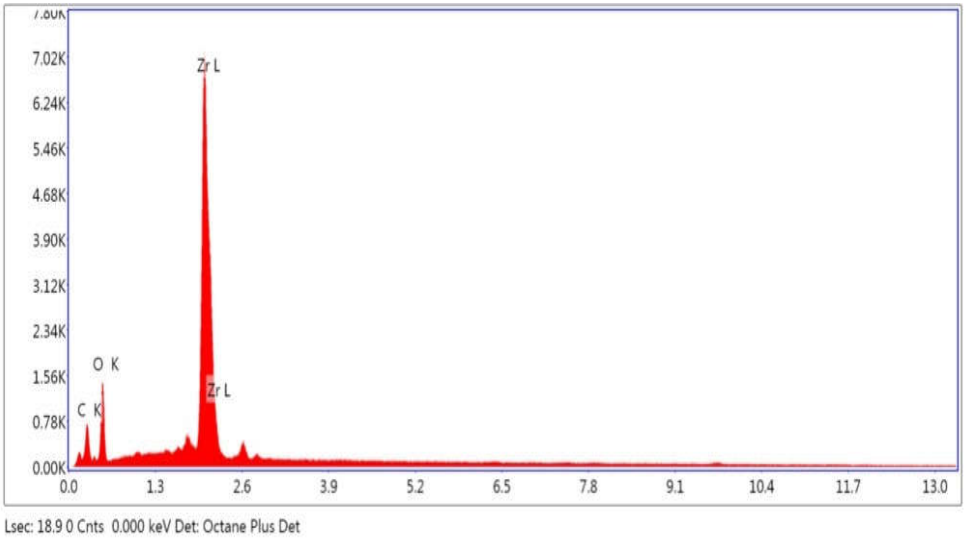

Figure 20: EDS of Zr MOF

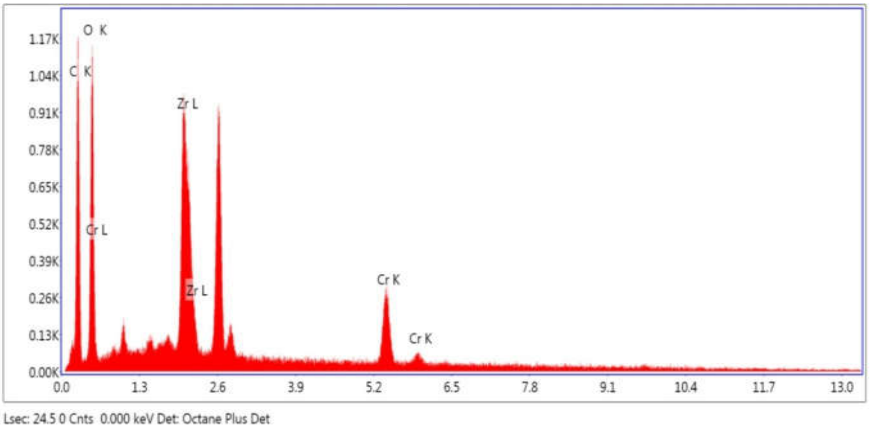

Figure 21: **EDS of Zr Cr MOF**

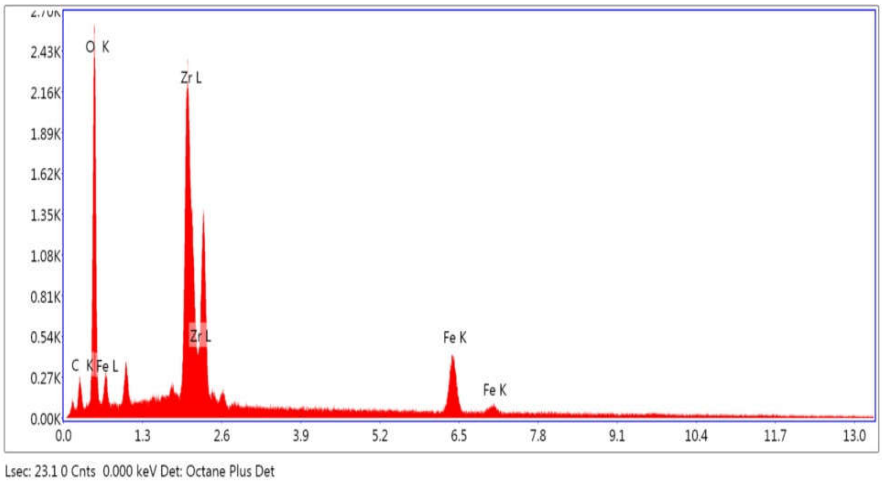

Figure 22: EDS of Zr Fe MOF

Table 2: Atomic Percentage of different Elements in MOFs

MOF	C	O	Zr	Cr	Fe
Fe-BDC	**65.1**	**34.7**			**0.2**
Cr-BDC	**53.62**	**40.33**		**6.05**	
CrFe-BDC	**32.18**	**46.53**		**16.32**	**4.97**
Zr-BDC	**48.6**	**40.9**	**10.5**		
ZrCr-BDC	**58.71**	**37.25**	**2.05**	**1.99**	
ZrFe-BDC	**21.4**	**68.5**	**6.02**		**4.07**

Solid state UV spectral studies

The peak observed at 313.8 nm in the UV spectrum of the ligand (Fig.23) correspond to π–π* transitions and peak at 244.5 represents n–π* transitions. The peak at 302.3 nm in Cr BDC MOF (Fig.24) is due to π–π* transitions and that at 241.9 nm is due to n–π* transitions depicting interactions with the ligand. Absorption in the visible region i. e; at 425.4 and at 578.7 nm is due to d-d transition in the metal [9].

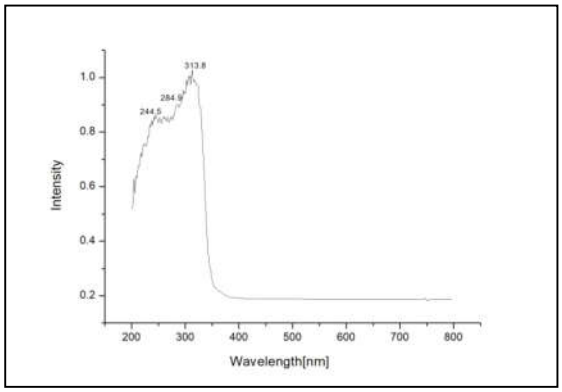

Figure 23: UV spectrum of 1,4-BDC

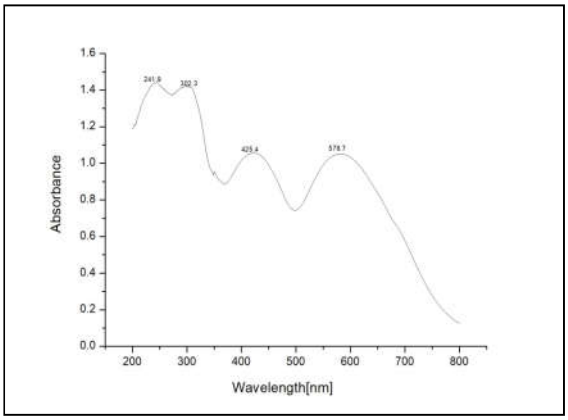

Figure 24: UV spectrum of Cr BDC MOF

The signal at 322.5 nm in Fe BDC MOF (Fig.25) is due to π–π* transitions and that at 237.3 nm corresponds to n–π* transitions showing interactions with the ligand. Signal in the visible region i.e; at 434.2 nm is due to d-d transition in the metal [9].

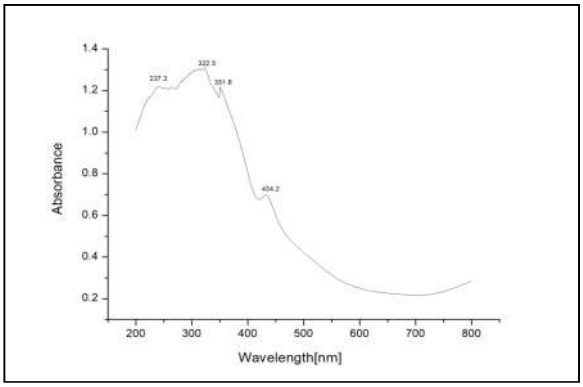

Figure 25: UV spectrum of Fe BDC MOF

The signal at 293.6 nm in Cr Fe BDC MOF (Fig.26) is due to π–π* and that at 234.4 nm is due to n–π* transitions showing interactions with the ligand. Signal in the visible region i.e; at 580.7 nm is due to d-d transition in the metal [9]. The peak at 295.95 nm is due to π–π* and that at 243.3 nm is due to n–π* transitions confirming interactions with the ligand in Zr BDC MOF (Fig. 27).

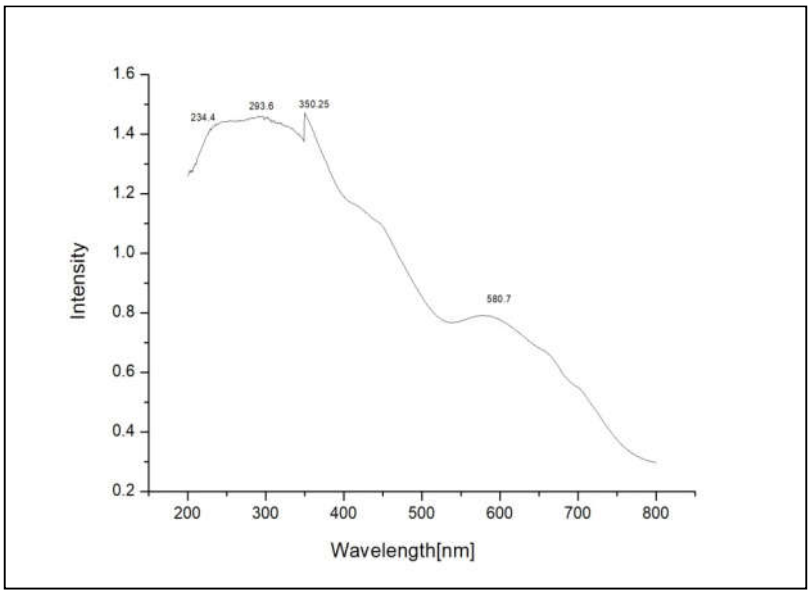

Figure 26: UV spectrum of Cr Fe BDC MOF

The signal at 301.17 nm in Zr Cr BDC MOF (Fig. 28) is due to π–π* and that at 241.69 nm is due to n–π* transitions showing interactions with the ligand. Signals in the visible region i.e; at 429.60 and at 605.82 nm are due to d-d transition in the constituent metals [9].

The peak at 291.08 nm in Zr Fe BDC MOF (Fig. 29) is due to π–π* and that at 249.52 nm is due to n–π* transitions showing interactions with the ligand. Signal in the visible region i.e; at 434.27 nm is due to d-d transition in the metal [9].

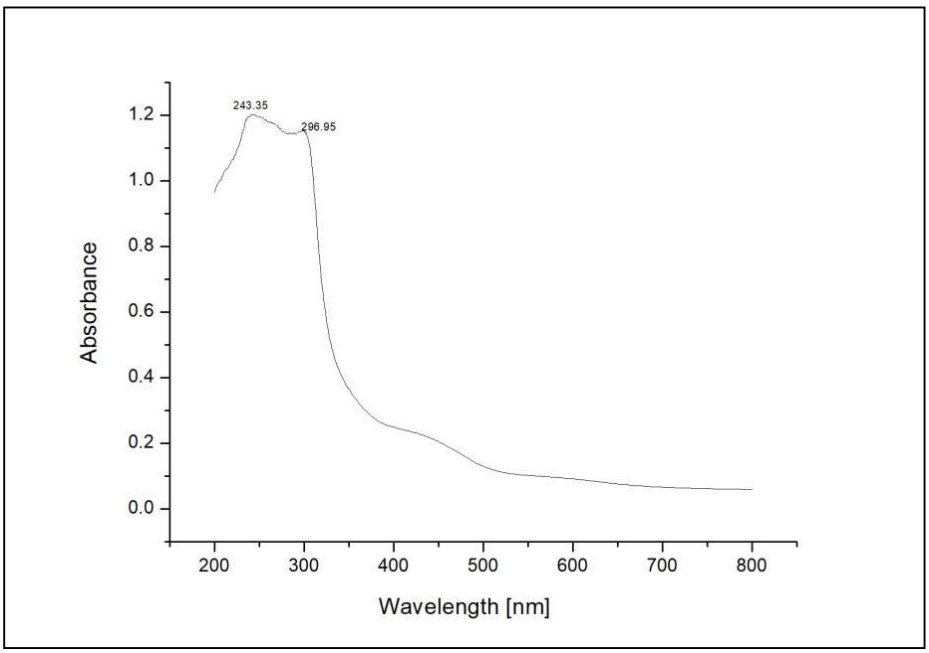

Figure 27: UV spectrum of Zr BDC MOF

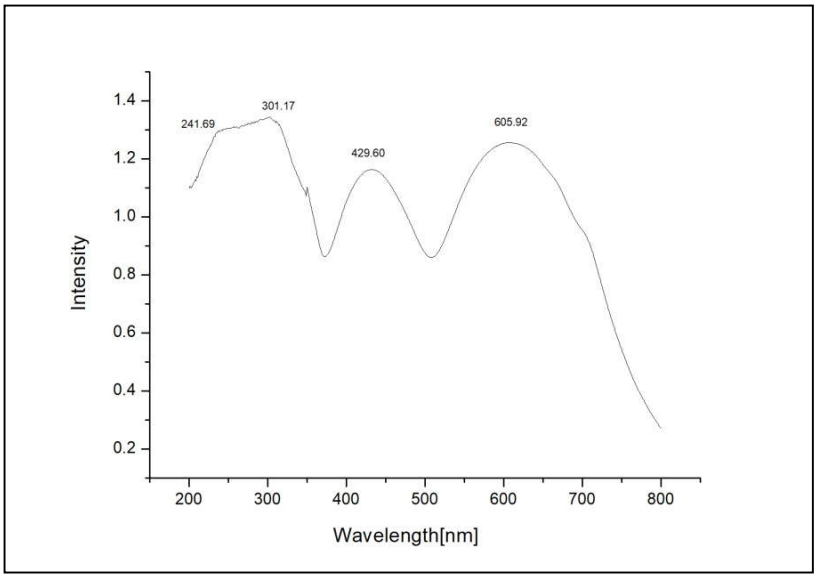

Figure 28: **UV spectrum of ZrCr BDC MOF**

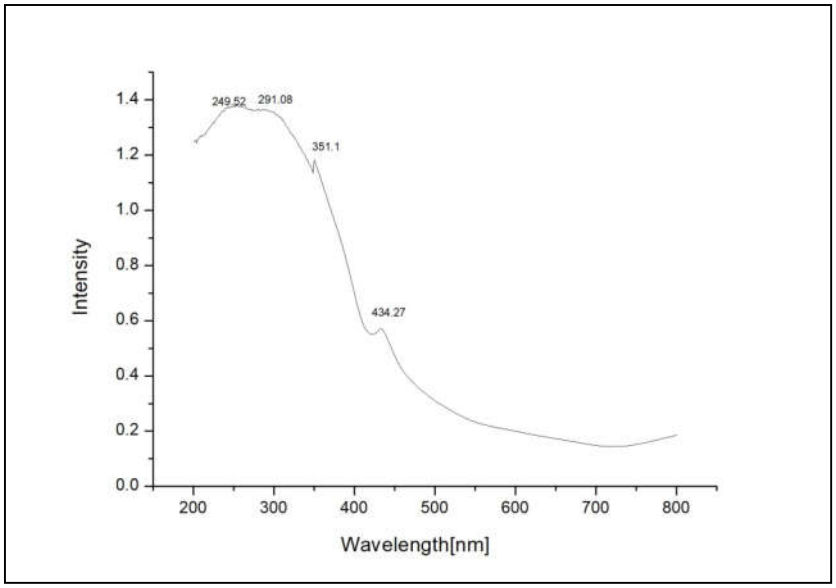

Figure 29: UV spectrum of Zr Fe BDC MOF

Photoluminescence Studies

Luminescent properties of the free ligand as well as those of MOFs were studied in the solid-state at room temperature. The free ligand emitted strong fluorescence centered at 492 nm (λ_{ex} = 430 nm) (Fig.30) and at 459, due to π-π* and n-π* transitions and also due to the unsaturation and conjugation in the ligand.

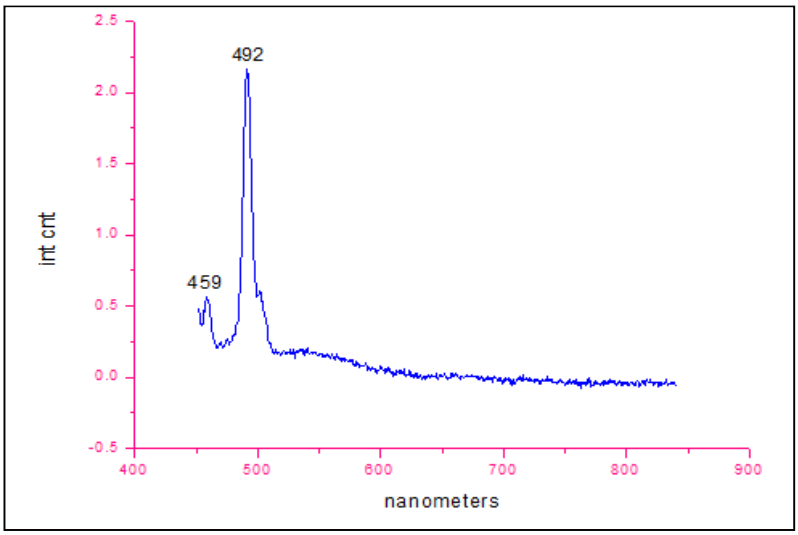

Figure 30: PL of 1,4-BDC excited at 430nm

In the PL spectrum of Cr BDC MOF (Fig.31), there are sharp peaks at 468.75, 482.59, 493.04, 575 and 684.89nm (λ_{ex} = 415 nm). In Cr^{3+} ions, upper ^2Eg to ^4A_2g ground state transition result in an emission at 640 nm[10]**.** It is red shifted to 684.89nm in the MOF. The ligand gave an intense emission peak at 459 nm upon excitation and is due to the intra ligand π-π* transition.

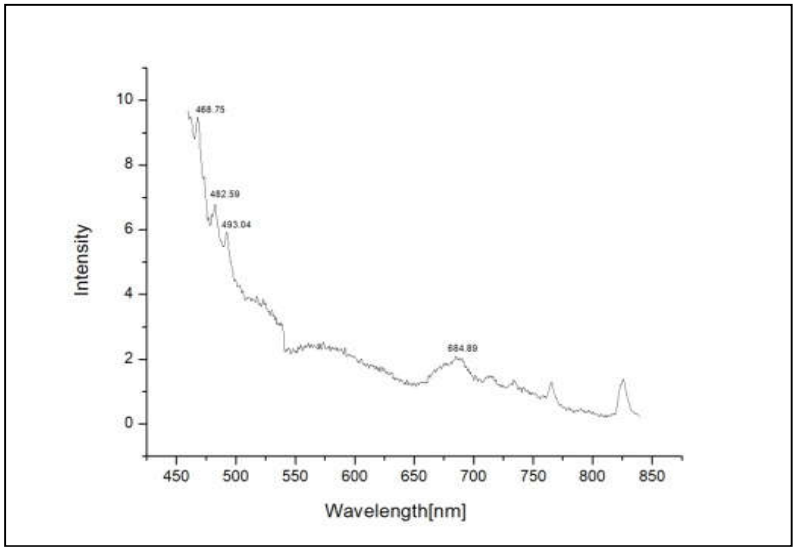

Figure 31: PL spectrum of CrBDC MOF (λex = 415 nm)

In the PL spectrum of FeBDC MOF (Fig.32), there are sharp peaks at 431.65, 467.27, 476.17, and 584.58nm (λex = 411 nm). The emission peak at 467.27 nm shows the intra-ligand π–π* transition. In the PL spectrum of Cr Fe BDC MOF (Fig.33), there are sharp peaks at 451.17, 462.46, 466.90, 480.75 and 493.3 nm (λ_{ex} = 350 nm). The signal at 462.7 nm represents the intra-ligand π–π* transition. The maximum emission peak observed at around 493 nm in the MOF is due to the intra ligand n–π* transition [10, 11].

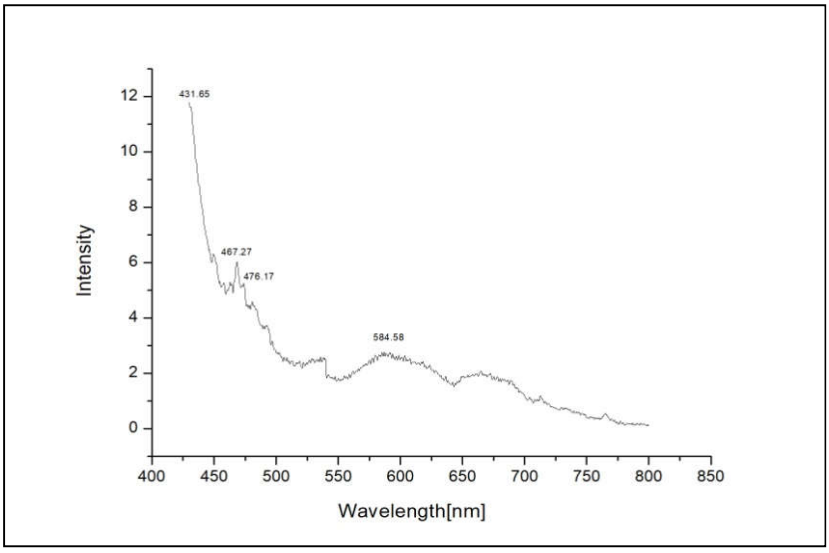

Figure 32: **PL spectrum of Fe BDC MOF (λex = 411 nm**)

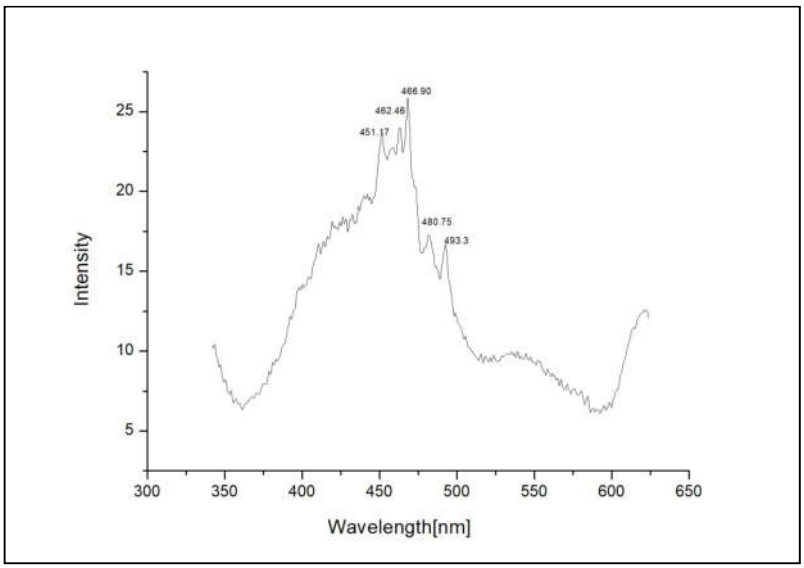

Figure 33: PL spectrum of CrFeBDC (λex = 350 nm)

In the PL of Zr-BDC (Fig.34) there are sharp peaks at 396.75, 451.27, 467.98, 482.24, 493.15 and 549nm. PL spectrum of Zr Cr BDC MOF (Fig.35) shows sharp peaks at 420, 449, 467.84, 492.38 and 541.56nm. The peak at 467.84 nm upon excitation is due to the intra ligand π–π* transition. The maximum wavelength observed at around 492.38 nm is due to the intra ligand n–π* transition[10-11]. The main signal around 420nm shows the transfer of one electron from the 2p orbital of oxygen to a 4d orbital of zircon [10-11].

.

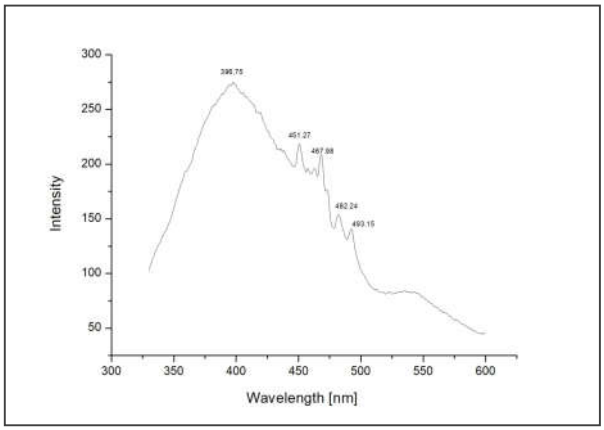

Figure 34: **PL spectrum of Zr BDC MOF (λex = 310 nm)**

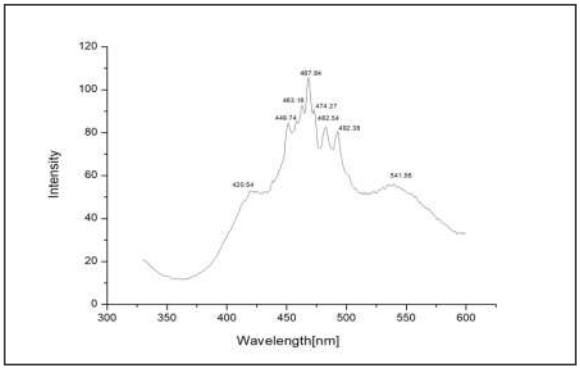

Figure 35: PL spectrum of Zr Cr BDC (λex = 240 nm)

In the PL of Zr Fe BDC MOF (Fig.36), there are sharp peaks at 420.89, 449.53, 461.7, 467.3 and 483.5 nm. The peak at 461.7 nm shows the intra-ligand π–π* transition.

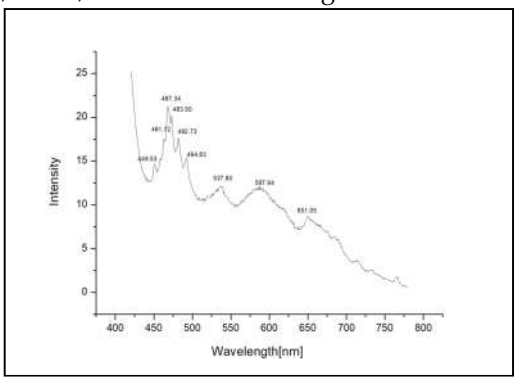

Figure 36: **PL spectrum of Zr Fe BDC (λex = 400 nm)**

Photocatalytic activity studies

The photocatalytic studies were conducted for the synthesized MOFs. Photocatalytic efficiency was analyzed based on hydrogen evolution on irradiation with visible light from a solar source. For Cr BDC MOF, significant photocatalytic activity and hydrogen evolution (Fig.37) was observed. It is promising to note that the synthesized MOF itself is capable of effective hydrogen production on solar illumination

without adding any cocatalysts. There is also no auxochrome attached to the organic linker to enhance efficiency [12].

A high rate of photo catalytic activity with large amount of hydrogen evolution is shown by Fe-BDC MOF (Fig.38). The efficiency is attributed to the direct excitation on the Fe-O clusters to induce electron transfer from oxygen anion to Fe cations. Among the synthesized MOFs, Fe BDC MOF shows the highest catalytic activity for hydrogen production [12].

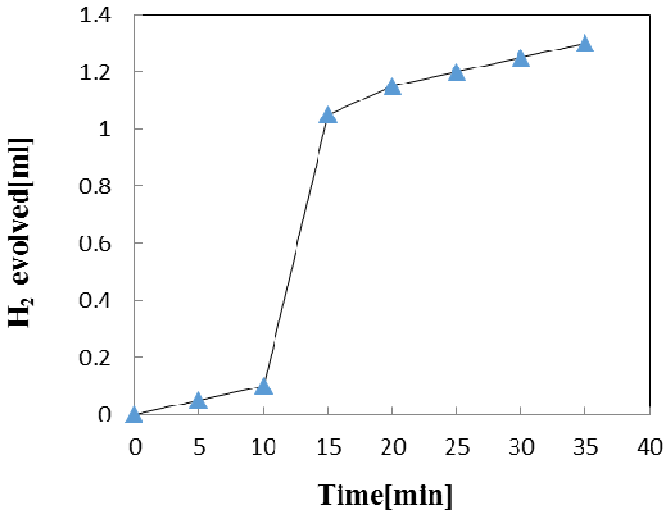

Figure 37: Photocatalytic evolution of hydrogen using Cr BDC MOF as catalyst during 4 hours light irradiation by solar simulator

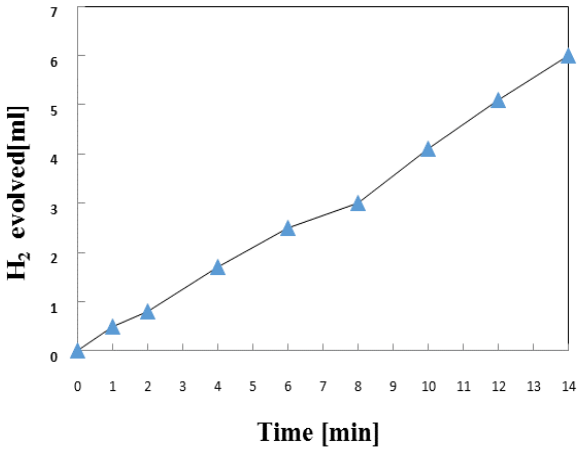

Figure 38: Photocatalytic evolution of hydrogen using Fe BDC MOF as catalyst during 4 hours light irradiation by solar simulator

The synthesized hetero bimetallic Cr Fe BDC MOF (Fig.39) also showed photo catalytic activity for hydrogen evolution. The activity shown by Cr Fe BDC MOF was found to be less compared to the constituent single metals but is also efficient to some extent. The as synthesized zirconium based MOFs did not show any photocatalytic activity. It is reported that Zr MOF show photocatalytic activity when irradiated with pyrex filtered UV source in methanol medium. Also, the presence of amino substituent as auxochrome in organic linker increases the efficiency [13-14].

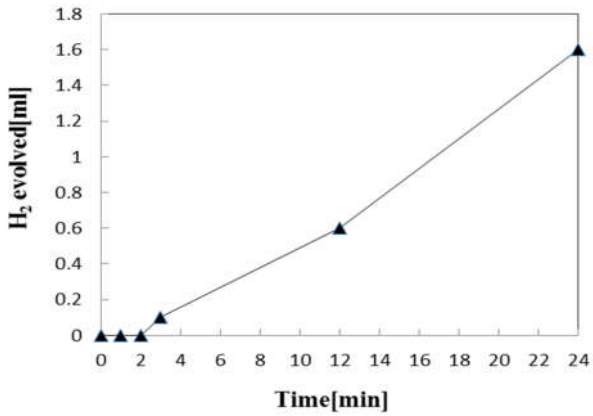

Figure 39: Photocatalytic evolution of hydrogen using Cr Fe BDC MOF as catalyst during 4 hours light irradiation by solar simulator

The transfer, migration, and recombination of the photogenerated electron-hole pairs are investigated by the PL emission spectrum technique in detail [15]. The MOFs give different broad emission bands with maximum intensities in the regions 460-493 nm (Figs. 31-33). PL emission intensity of FeBDC MOF was comparatively lower than that of other two MOFs, which offers useful evidence for the greatly suppressed photogenerated electron recombination through the π-π interactions of other MOF photocatalysts[16]. The possible mechanism for high photocatalytic H_2 evolution of MOFs is under the visible light irradiation, the electrons (e^-) at valence band (VB) could be stimulated to the conduction band (CB) of MOFs, the CB electrons of MOFs reduce H^+ in water to generate H_2.

CONCLUSIONS

We have successfully synthesized three MOFs and three hetero-bimetallic MOF-photocatalysts with 1,4-BDC as the ligand. The Fe BDC MOF showed the highest amount of hydrogen evolution, without adding any cocatalyst and photosensitizer. 0.2 g Fe MOF gave 6mmol H_2 from 20 mL of water. Zirconium based MOFs did not show any photocatalytic activity under the current experimental conditions.

REFERENCES

1. Tella, A. C., & Aaron, I. Y. (2012). Syntheses and applications of metal-organic frameworks materials: A review. *Acta Chimica Pharmaceutica Indica*, *2*(2), 75–81.
2. Chen, S., Lucier, B. E. G., Chen, M., Terskikh, V. V., & Huang, Y. (2018). Probing calcium-based metal-organic frameworks via natural abundance ^{43}Ca solid-state NMR. *Chemistry – A European Journal*, *24*, 8732–8736.
3. Bo, Q.-B., Zhang, H.-T., Wang, H.-Y., Miao, J.-L., & Zhang, Z.-W. (2014). Anhydrous lanthanide MOFs and direct photoluminescent sensing for polyoxometalates in aqueous solution. *Chemistry – A European Journal*, *20*, 3712–3723.
4. Takanabe, K. (2017). Photocatalytic water splitting: Quantitative approaches toward photocatalyst by design. *ACS Catalysis*, *7*, 8006–8022.
5. Song, F., Li, W., & Sun, Y. (2017). Metal–organic frameworks and their derivatives for photocatalytic water splitting. *Inorganics*, *5*(3), 40.
6. Wang, Y., Li, L., Dai, P., Yan, L., Cao, L., Gu, X., & Zhao, X. (2017). Missing-node directed synthesis of hierarchical pores on a zirconium metal–organic framework with

tuneable porosity and enhanced surface acidity via a microdroplet flow reaction. *Journal of Materials Chemistry A*, *5*, 22372–22379.

7. Chatterjee, A., Hu, X., & Leung–Yuk Lam, F. (2018). Towards a recyclable MOF catalyst for efficient production of furfural. *Catalysis Today*, *314*, 129–136.
8. Ghanbarian, M., Zeinali, S., & Mostafavi, A. (2018). A novel MIL-53(Cr-Fe)/Ag/CNT nanocomposite based resistive sensor for sensing of volatile organic compounds. *Sensors and Actuators B: Chemical*, *213*, 381–391.
9. Alfonso-Herrera, L. A., Huerta-Flores, A. M., Torres-Martínez, L. M., Rivera-Villanueva, J. M., & Ramírez-Herrera, D. J. (2018). Hybrid $SrZrO_3$-MOF heterostructure: Surface assembly and photocatalytic performance for hydrogen evolution and degradation of indigo carmine dye. *Journal of Materials Science: Materials in Electronics*, *29*, 10395–10410.
10. Lachheb, R., Herrmann, A., Damak, K., Rüssel, C., & Maâlej, R. (2017). Optical absorption and photoluminescence properties of chromium in different host glasses. *Journal of Luminescence*, *186*, 152–157.
11. Shi, L., Wang, T., Zhang, H., Chang, K., Meng, X., Liu, H., & Ye, J. (2015). An amine-functionalized iron (III) metal–organic framework as efficient visible-light photocatalyst for Cr (VI) reduction. *Advanced Science*, *2*, 1500006.
12. Gomes Silva, C., Luz, I., Llabrés i Xamena, F. X., Corma, A., & García, H. (2010). Water stable Zr–benzene dicarboxylate metal–organic frameworks as photocatalysts for hydrogen generation. *Chemistry – A European Journal*, *16*, 11133–11138.
13. Wen, M., Mori, K., Kuwahara, Y., An, T., & Yamashita, H. (2017). Design and architecture of metal organic frameworks for visible light enhanced hydrogen production. *Applied Catalysis B: Environmental*, *218*, 555–569.
14. He, J., Yan, Z., Wang, J., Xie, J., Jiang, L., Shi, Y., Yuan, F., Yu, F., & Sun, Y. (2013). Significantly enhanced photocatalytic hydrogen evolution under visible light over CdS embedded on metal–organic frameworks. *Chemical Communications*, *49*(60), 6761–6763.
15. Wang, D., Huang, R., Liu, W., Sun, D., & Li, Z. (2014). Fe-based MOFs for photocatalytic CO_2 reduction: Role of coordination unsaturated sites and dual excitation pathways. *ACS Catalysis*, *4*(12), 4254–4260.
16. Yuan, Y. P., Yin, L. S., Cao, S. W., Xu, G. S., Li, C. H., & Xue, C. (2015). Improving photocatalytic hydrogen production of metal–organic framework UiO-66 octahedrons by dye-sensitization. *Applied Catalysis B: Environmental*, *168*, 572–576.

****